RSC Advances

This is an *Accepted Manuscript*, which has been through the Royal Society of Chemistry peer review process and has been accepted for publication.

Accepted Manuscripts are published online shortly after acceptance, before technical editing, formatting and proof reading. Using this free service, authors can make their results available to the community, in citable form, before we publish the edited article. This *Accepted Manuscript* will be replaced by the edited, formatted and paginated article as soon as this is available.

You can find more information about *Accepted Manuscripts* in the Information for Authors.

Please note that technical editing may introduce minor changes to the text and/or graphics, which may alter content. The journal's standard Terms & Conditions and the Ethical guidelines still apply. In no event shall the Royal Society of Chemistry be held responsible for any errors or omissions in this *Accepted Manuscript* or any consequences arising from the use of any information it contains.

ROYAL SOCIETY OF CHEMISTRY

www.rsc.org/advances

Table of contents

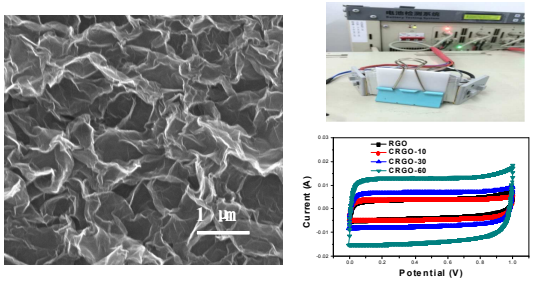

Freestanding 3D mesoporous graphene with enhanced capacitance for supercapacitors has been synthesized by carbon monoxide reduction, healing and activation.

RSC Advances Accepted Manuscript

Freestanding 3D mesoporous graphene oxide for high performance energy storage applications

Zijiong Li[a] *,Baocheng Yang[b], Kun Li[b], Haiyan Wang[a], Xiaowei Lv[b], Yanzhen Guo[b], Zhifeng Zhang[a], Yuling Su[a]

[a] *School of Physics & Electronic Engineering, Zhengzhou University of Light Industry, Zhengzhou, 450002, PR China*

[b]*Institute of Nano Functional Materials, Huanghe University of Science & Technology, Zhengzhou 450006, PR China*

*Corresponding author:

zijiongli@zzuli.edu.cn (Zijiong Li)

RSC Advances Accepted Manuscript

Abstract

We report a novel thermal reduction process to obtain excellent electrical conductivity, freestanding 3D mesoporous graphene for supercapacitor electrode applications in the presence of CO atmosphere. The introduction of CO can not only effectively reduce and repair graphene oxide (GO) with fewer defects, but also activates graphene with highly mesoporous nanostructures. The CO-activated thermal graphene oxide (CRGO) exhibits enhanced specific capacitance of 291 Fg^{-1} at a current density of 1 Ag^{-1}, high rate capability, and excellent cycle performance compared to conventional thermal reduction GO. The method demonstrated that the help of CO is an efficient way for the improvement of the supercapacitive performance during thermally reduced graphene oxide.

Keywords: Graphene; Supercapacitor; Electrochemical performance

RSC Advances Accepted Manuscript

1. Introduction

Supercapacitors and lithium ion batteries are the two important electrochemical energy storage devices for the sustainable energy supply in near future.[1-3] With the unique features like fast charging/discharging rate, long cycle life and high power density, supercapacitors have generated great interest in consumer electronics, hybrid electric vehicles, and industrial power management.[4-7] However, supercapacitors store much less energy than batteries which limits their practical applications. Hence, great efforts have been made to enhance the capacitor performance including developing and optimizing the electrode materials. Graphene, as a novel two-dimensional carbon material, has been widely investigated for electrochemical energy storage due to its many unusual features, including superior electrical conductivity, excellent mechanical flexibility, large specific surface area, and high thermal and chemical stability. Graphene-based supercapacitors could achieve specific capacitance as high as 550 Fg^{-1} in principle, which is a higher value than other carbon-based materials for supercapacitors. [8-10]

Various methods of preparing graphene have been explored for use in supercapacitors, such as micromechanical cleavage, chemical vapor deposition, epitaxial growth on SiC, and chemical or thermal reduction of graphene oxide (GO). Especially, graphene-based materials derived from thermal reduction of GO can be manufactured on the ton scale at low cost, making them potentially cost-effective materials for supercapacitor.[11-14] The reduction level of GO can be precisely controlled by the annealing temperature, the duration, and the atmosphere. However,

RSC Advances Accepted Manuscript

thermal reduced GO often suffers from irreversible sheet-to-sheet restacking due to the strong van der Waals force, which not only greatly reduces the ion accessible surface area, but also brings large ion diffusion resistance between the adjacent graphene sheets. In addition, defects detrimental to the conductivity are also generated during the chemical or thermal treatment. Therefore, simple methods to mass production of high-quality graphene with fewer defects for application in supercapacitors are highly desired.

To date, a great deal of effort has been devoted to enhancing capacitive performance of graphene by modifying its texture and surface such as introducing a spacer into graphene sheets. Metal nanoparticles, metal oxide nanoparticles, and various carbon materials (i.e., carbon nanotubes, carbon black, etc) have been used as spaces to intercalate in between the graphene sheets. Such composites show an improved electrochemical capacitive performance compared to only graphene due to not only larger surface area but also pseudocapacitance introduced by metal or metal oxide nanomaterials.[15-20] However, a drastic decay has been observed at high discharging rates in this case which may be due to their poorer electrical conductivity. On the other hand, porous graphene that provides short diffusion paths to significantly improve the overall supercapacitive performances has generated increasing interest.[21-24] Ruoff et al have reported the usage chemical activation of microwave exfoliated graphene oxide with KOH to preparation of porous graphene with extremely high surface area up to 3100 m^2g^{-1}.[25] Such porous graphene exhibits a very good performance as supercapacitors electrodes. Other approaches to synthesis of

RSC Advances Accepted Manuscript

porous graphene have reported by using template such as MgO to create nanopores on graphene planes to avoid the restacking of the graphene sheet and thereby improve the supercapacitive performance.[26-28] These synthesis processes often require complex steps, harsh conditions and a series of post-processing procedures. Therefore, the development of a facile method to obtain graphene with highly porous and fewer defects is still a challenge.

In this work, we demonstrate a template-free one step procedure for the synthesis of freestanding 3D GO with high mesopores, excellent conductivity and few defects by CO-activated thermal graphene oxide (CRGO). The CRGO electrode materials with outstanding rate capability, specific capacitance, and cycle stability are superior to conventional thermal reduction of graphene oxide (RGO). These high electrochemical performances make these high quality CRGO materials very attractive for application in electrochemical energy storage.

2. **Experimental**

2.1 Synthesis of samples

GO was synthesized from natural graphite powders by a modified Hummers method (supplementary information). As synthesized GO (0.09 g) was then dispersed in water to create a dispersion (0.5 mg mL^{-1}). After filtration and freeze-drying, the sample was placed in a horizontal quartz tubular reactor, and heated from room temperature to 900 ^{o}C at 20 °C min^{-1} under Ar (99.999%) atmosphere with a flow rate of 300 mL min^{-1}. Subsequently, CO gas (99.95%) was introduced in turn at the same temperature with a flow rate of 5 mL min^{-1} and kept for 10 min (CRGO-10), 30 min

RSC Advances Accepted Manuscript

(CRGO-30), and 60 min (CRGO-60), respectively. Finally the system was cooled down to room temperature in Ar atmosphere.

For comparison, the same method was used to synthesize thermal reduction of graphene oxide (RGO) in the absence of carbon monoxide gas.

2.2 Characterization

Powder X-ray diffraction (XRD) analyses were performed on a Bruker D8 ADANCE diffractometer with Cu-Kα radiation. X-ray photoelectron spectroscopy (XPS) spectra were collected on an AXIS ULTRA spectrometer. Raman spectra were obtained from all samples using Renishaw inVia Raman microscope with an excitation wavelength of 532 nm. The morphologies of the as-obtained samples were observed by a field-emission scanning electron microscopy (FESEM, Quanta 250 FEG) and transmission electron microscope (TEM, JEOL JEM-2100). The chemical compositions of the synthesized samples were determined by an Elementar Vario EL CHNS analyzer. The nitrogen adsorption/desorption isotherms were measured at 77 K on Quantachrome analyzer. The specific surface area was obtained by Brunauer–Emmett–Teller (BET) analyses of the adsorption isotherms. The pore size distribution curves were calculated from the adsorption branch using the nonlocal density functional theory model assuming the slit pore geometry. The electrical conductivity of the samples was measured by the four-point probe method (Mitsubishi, Japan).

2.3 Electrochemical Measurements

The electrochemical measurements, including cyclic voltammograms (CVs), galvanostatic charge/discharge, and electrochemical impedance spectroscopy were

RSC Advances Accepted Manuscript

performed in a three-electrode setup with 6 M KOH aqueous solution as electrolyte. A Ni foam coated with the active materials served as the working electrode, platinum foil electrode, and a saturated calomel electrode (SCE) served as the counter and reference electrodes, respectively. The working electrode was prepared by mixing an active material (90 wt%) with polytetrafluoroethylene (5 wt.%) and carbon black (5 wt.%) in water. The slurry of the mixture was painted between two pieces of Ni foam (1cm×1cm) suspension and compressed before measurement. The mass loading for each electrode is ~1.5 mg cm^{-2}. In a two-electrode configuration, a cell with two symmetric working electrodes was configured and Celgard 3501 membrane was used as the separator, with 1.0 M tetraethylammonium tetrafluoroborate ($TEABF_4$) in acetonitrile (AN) as electrolyte. The electrochemical measurements were carried out on a CHI 660D (Chenhua, Shanghai) electrochemical workstation at room temperature. A Xinwei battery testing equipment (Shenzhen, China) was used to run the galvanostatic charge/discharge cycles.

3. Results and Discussion

3.1 Morphological and structural characterizations

Morphology of GO and CRGO were characterized by optical, scanning electron microscopy (SEM), transmission electron microscopy (TEM) images in Fig.1. As shown in Fig.1a, a huge volume expansion can be observed during transformation from GO to CRGO. It is indicated the change in color from golden brown to black. The GO sample (Fig.1b) exhibits compact bulk morphology. After CO treated at 900 ^{o}C for 10 and 30 min, typical aggregates of wrinkled layered structures are still

RSC Advances Accepted Manuscript

observed (Fig.S1). After treated for 60 min, the CRGO exhibits a freestanding 3D honeycomb-like nanostructure (Fig.1c). Numerous exterior pores can be clearly identified among the graphene sheets, providing a large accessible area (Fig.1d). A single layer or a few layers of CRGO sheets were crumpled and wrinkled with time of thermal treatment increasing. A great deal of pores is also confirmed by TEM observation (Fig.1e). The HRTEM microphotograph shown in Fig.1f, which was taken on the edge of a CRGO nanosheet, clearly reveals that the porosity is made up of randomly oriented narrow pores.

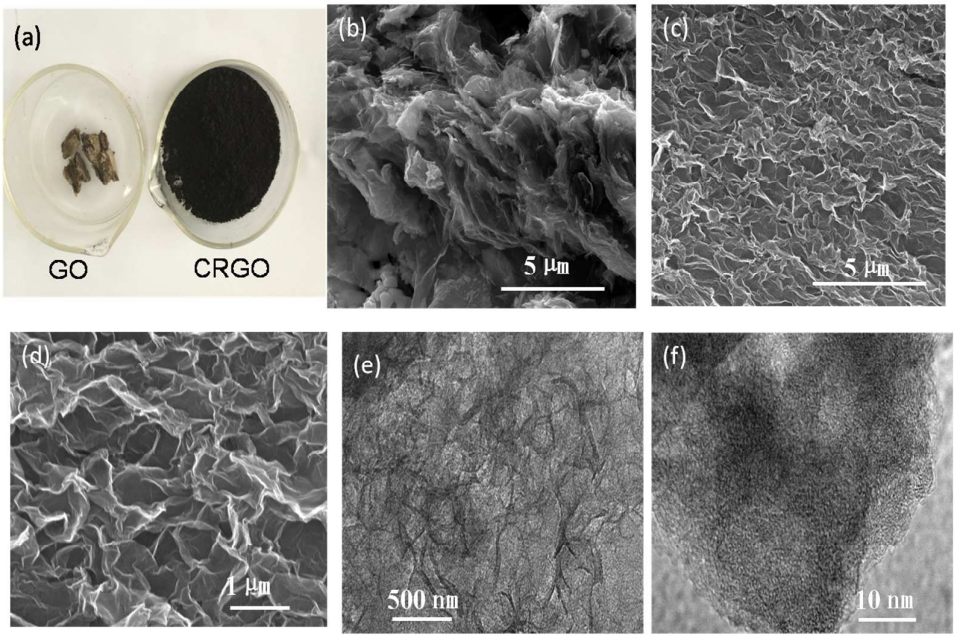

Fig.1 Morphologies characterization of CRGO.(a) optical images of the GO and resulted CRGO. (b) SEM image of GO. (c) Low- and (d) high-magnification SEM images of CRGO. (e) Low- and (d) HRTEM images of CRGO.

To investigate the effect of CO treated GO, X-ray photoemission spectroscopy

RSC Advances Accepted Manuscript

(XPS), X-ray diffraction (XRD), and fourier transform infrared (FT-IR) were used to characterize the chemical structure and composition of the samples. As is shown in Fig.2a, C1s components of GO are assigned to C-C, C-O and C=O, respectively. After it was reduced and repaired by CO, the C1s peak associated with C-C (284.6 eV) became predominant (Fig.2b), while the peaks related to the oxidized carbon species (C=O, C-O epoxy/ether) were greatly weakened or disappeared. The recovery of conjugated system from GO upon reduction was also confirmed by the XRD patters (Fig.2c). After oxidation, the (0 0 2) peak of graphite powder disappears and an additional peak at ~11° is observed, which is corresponding to the (0 0 1) diffraction peak of GO. According to the following formula:

$$n\lambda=2d\bullet\sin\theta \quad (1)$$

Where λ is the wavelength of incident x-rays, θ is the angle of incidence and n is the integer (n=1). The d-spacing of GO increased to 0.779 nm from 0.335 nm of graphite powder, which is ascribed to the oxide-induced O-containing functional groups and inserted H_2O molecules. After thermal treatment in the presence of CO atmosphere, the diffraction peak of GO disappeared and the graphene displayed a weak, broad diffraction peak of (002) diffraction at ~ 24.5° (d-spacing ~0.363 nm), which indicates an efficient reduction of the GO and a high degree of exfoliation of the layered graphene sheets. These results can be also confirmed by FT-IR. As shown in Fig. 2d, the FTIR spectrum of GO at 1728 cm^{-1} corresponds to C=O stretching vibration, 3406 cm^{-1} for O-H stretching vibration, 1052 cm^{-1} for C-O stretching, and 1612 cm^{-1} for skeletal vibration from unoxidized graphite domain.[29] After CO

RSC Advances Accepted Manuscript

reduction and reparation, these oxygen-containing functional groups derived from the intensive oxidation were reduced significantly. The peaks for O-H and C-O are almost entirely removed, reflecting the highly reduced of GO.

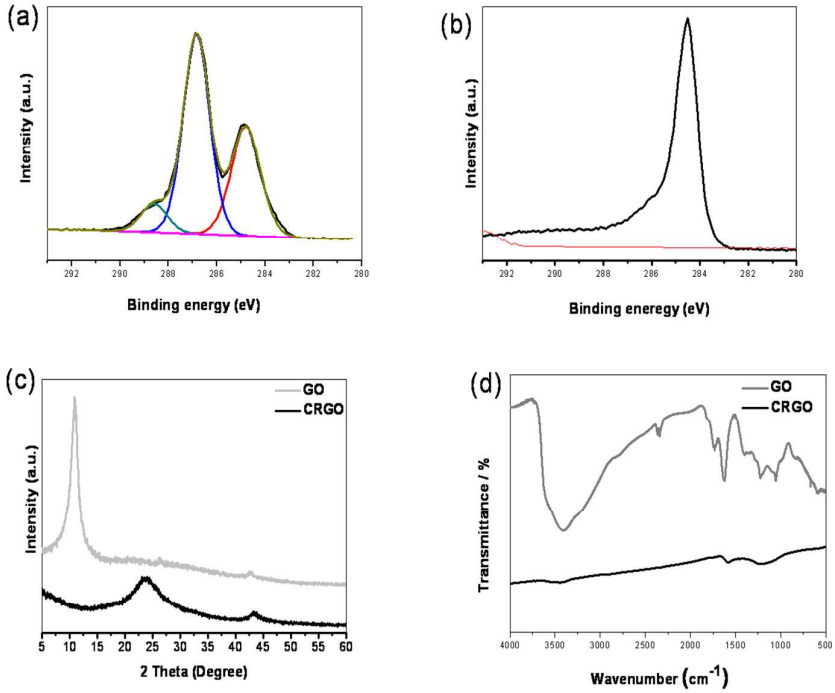

Fig.2 Structure characterization of CRGO (a) High resolution C1s spectra of GO and (b) CRGO. (c) XRD patterns and (d) FTIR spectra of GO and CRGO.

Information about the structure of CRGO was further verified by analysis of Raman spectra. Two typical peaks appeared at ~1580 cm^{-1} (G-peak) arising from the first order scattering of the E_{2g} phonon of sp^2 C atoms, D-peak (~1350 cm^{-1}) arising from a breathing mode of photons of A_{1g} symmetry. [30] The D-peak is related to the amount of disorder and its intensity shows the degree of edge chirality. Generally, the intensity ratio of D and G peaks (I_D/I_G) of samples indicated the degree of the disorder such as defects, ripples and edges. [31, 32] As shown in Fig.3, the I_D/I_G gradually

RSC Advances Accepted Manuscript

decreased from 1.73 (GO) to 0.64 (CRGO-60) and the G-peak for GO (~1605 cm^{-1}) was shifted to ~ 1590 cm^{-1} (graphite, 1580 cm^{-1}) indicating that the sp^2 domains of conjugated carbon atoms were formed and recovered the hexagonal network of carbon atoms with defects during CO reduction and reparation.[31, 32] In addition, the I_D/I_G ratio is decreased with the time of CO gas treatment increasing. It is noteworthy that a new 2D band (~2700 cm^{-1}) of CRGO-60 appeared, indicating a thin layer of globally good quality after CO repaired for 60 min.

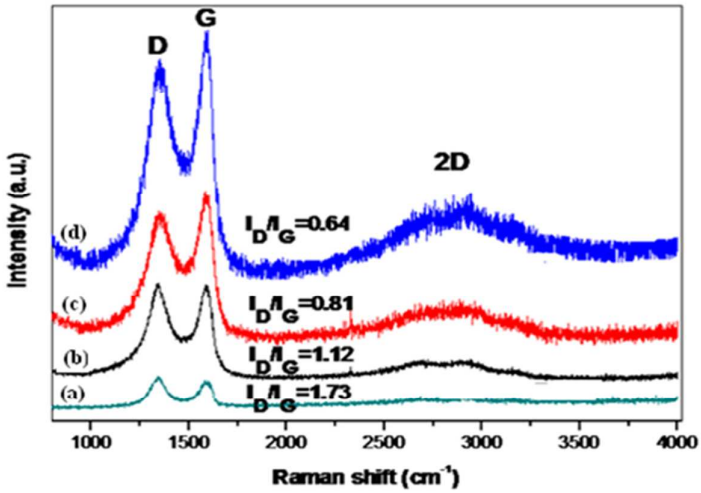

Fig.3 Raman spectra of (a) GO, (b) CRGO-10, (c) CRGO-30, and (d) CRGO-60.

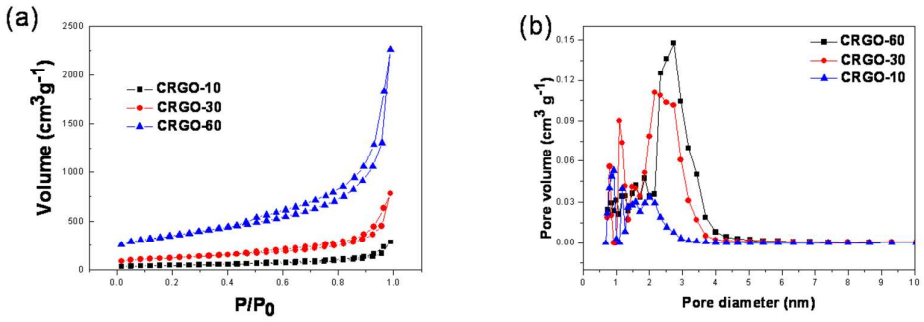

Fig.4 a) nitrogen adsorption/desorption isotherms of CRGO-10, CRGO-30, and CRGO-60, (b) pore size distributions of CRGO-10, CRGO-30, and CRGO-60

RSC Advances Accepted Manuscript

Nitrogen adsorption-desorption isotherms measurements were carried out for examining the specific surface area and pore volume of CRGO. The N_2 sorption isotherm and the pore size distribution of CRGO-10, CRGO-30 and CRGO-60 are shown in Fig.4a, b, respectively. The BET specific surface area of CRGO-60 is 1219 m^2g^{-1} and it has pores of sizes between 2.6-3.5 nm, demonstrating a mesopores structure. Due to the large number of structural porosity, the CRGO-60 exhibits a large pore volume of 5.3 cm^3g^{-1} (Table 1). This specific surface area and pore volume value are higher than that of thermal reduction (RGO) (305.1 m^2g^{-1}, 2.5 cm^3g^{-1}) without CO gas at the same condition, and significantly higher than that of CRGO-10 and CRGO-30. This comparison demonstrates the advantages of present CO activated route to producing highly porous graphene with large accessible surface area.

Table 1 The C/O atomic ratio, surface area, pore volume, and electric conductivity of GO, RGO, CRGO-10, CRGO-30 and CRGO-60.

Samples	C/O atom ratio	Surface area(m^2g^{-1})	Pore volume(cm^3g^{-1})	Electrical conductivity (S m^{-1})
GO	3.6	45.2	0.7	3.3×10^{-2}
RGO	19.8	305.1	2.5	5.6×10^{2}
CRGO-10	8.9	124.5	1.1	1.1×10^{2}
CRGO-30	11.2	427.3	2.8	2.8×10^{2}
CRGO-60	24.3	1218.5	5.3	1.5×10^{3}

The C/O atomic ratio, surface area, pore volume, and electric conductivity of GO, RGO and CO gas treatment at different time were summarized in Table 1. The C/O

RSC Advances Accepted Manuscript

atomic ratio of CRGO-60 (24.3) is higher than that of RGO (19.8), indicating the high level of the reduction and reparation. For CRGOs, C/O atomic ratio are strongly affected by the treatment time. Moreover, the electrical conductivity of CRGO-60 (1.5×10^3 Sm^{-1}) is higher than that of RGO (5.6×10^2 Sm^{-1}) at the same thermal treatment time due to the thermal restoration of the aromatic graphitic structure under CO atmosphere.

3.2 Electrochemical properties

In order to explore the energy storage application of the CRGO, we first investigate their electrochemical properties by a three-electrode setup with 6.0 M KOH aqueous solution. Fig.5a compares the CV profiles of CRGO-10, CRGO-30, and CRGO-60 with RGO at a scan rate of 5 mVs^{-1}. All CV curves show a perfect symmetrical rectangular shape, which indicates pure electrical double layer capacitance (EDLC) behavior.[33, 34] Compared with RGO, enlarged CV area of CRGO-60 corresponds to storage of a great amount of charge, indicating the capacitance of graphene is enhanced after CO activation. The good capacitive behavior of CRGO was also confirmed by galvanostatic charge/diacharge curves, as shown in Fig.5b. The perfectly symmetric charge/discharge curve of CRGO-10, CRGO-30, and CRGO-60 revealed a capacitive behavior of EDLC.

RSC Advances Accepted Manuscript

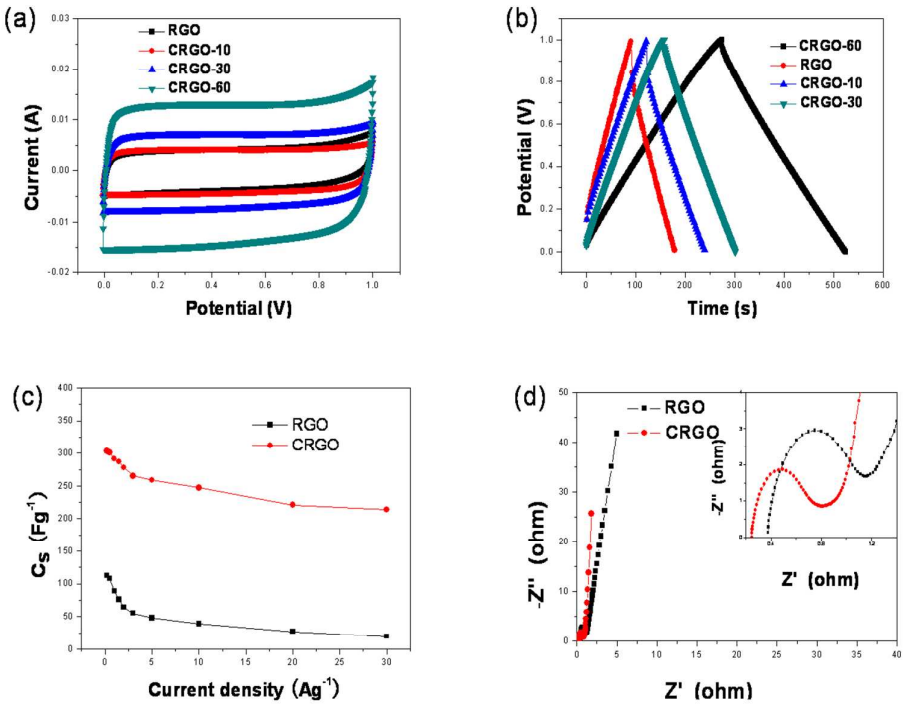

Fig.5 (a) CV curves at a scan rate of 200 mV/s. (b) Galvanostatic charge-discharge curves and ragone plots of CRGO-10, CRGO-30 and CRGO-60. (c) variation of specific capacitance against current density, and (d) Nyquist plots. Inset shows the magnified high-frequency regions.

The specific capacitance for the electrodes can be obtained from charge/discharge data according to the following equation.

$$C_s = \frac{I}{m \cdot \frac{dV}{dt}} \quad (1)$$

Where C_s is the specific capacitance (Fg^{-1}), I is current (A), dV/dt is the discharge slope after the IR drop, and m is the mass of the single electrode materials (g). The CRGO-60 displayed a higher specific capacitance of 291 Fg^{-1} at a current

RSC Advances Accepted Manuscript

density of 1.0 Ag^{-1}, which is greater than that of CRGO-10 (112 Fg^{-1}), CRGO-30 (143 Fg^{-1}), and RGO (89 Fg^{-1}). It should be noted that this value outperforms most of graphene (template-free method) electrode with described previously (Table S1). To evaluate the rate capability of the CRGO, specific capacitance was measured while varied the current density. Capacitance retention of CRGO-60 was 73.5 % from current density range from 1.0 Ag^{-1} to 30 Ag^{-1}, which is much greater than that of RGO (21.3 %). This behave can be attributed to the unique structural properties of CRGO, which combine a thin layer and wide mesopores that improve the ion diffusion rates, and a good electronic conductivity, which provides high electron transport rates. [35-40] Fig.5d shows the impedance spectra of RGO and CRGO-60 electrode material analyzed using Nyquist plots at applied potential of 0.4 V, over the frequency range between 10 kHz and 0.1 Hz. It shows a straight line in the low-frequency region and a semicircle in the high frequency region. At low frequency, the imaginary part sharply increases and a vertical line is usually observed, indicating a pure capacitive behavior. The internal resistance of CRGO-60 is smaller than that of RGO, which suggests that the CRGO materials have better conductive properties and, therefore, better electrochemical behavior. [41- 44] It is speculated that the low resistances of CRGO electrode is due to its highly porous structures and high surface areas, which facilitates a faster ion insertion and extraction during the charge/discharge process.

RSC Advances Accepted Manuscript

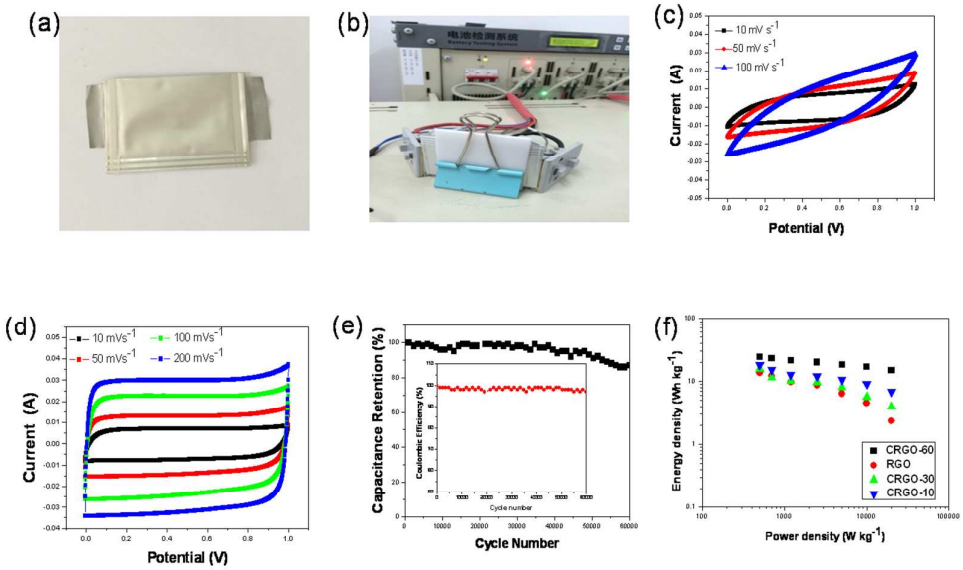

Fig.6 Capacitive performance of two-electrode capacitor. (a) Optical image of a symmetric two-electrode configuration, and (b) the capacitor charge/discharge testing, (c) CV curves at different scan rates of RGO and (d) CRGO-60. (e) The capacity retention of CRGO-60 as a function of cycling number. The inset shows the coulombic efficiency of CRGO-60 as a function of cycling number. (f) Ragone plots of CRGO-10, CRGO-30 and CRGO-60 and RGO based supercapacitors.

We further investigated the electrochemical and capacitive properties of CRGO by a symmetric two-electrode configuration. Fig.6a and b are the optical images of the electrode configuration and the charge/discharge testing, respectively. Symmetrical two-electrode supercapacitors were fabricated by separating two identical electrodes of CRGO, and their electrochemical performances were evaluated by CV and galvanostatic charge/diacharge. Fig.6c and d are the CV curves for RGO and CRGO-60 at various scan rates. The CV curves of RGO were highly compressed

RSC Advances Accepted Manuscript

under all scan rates. However, the CVs of CRGO-60 retain a rectangular-like shape with much less distortion even at high scan rates, indicating a good charge propagation within the electrode and the quick response of EDLC with a pure electrostatic character. As the stability of supercapacitors plays a vital role in real applications, [45, 46] the CRGO-60 based supercapacitor was evaluated under consecutive charge/discharge cycles. As shown in Fig.6 e, the capacity retention is measured to be about 87 % after repeating charge/discharge cycles for 60,000 times. Moreover, the coulombic efficiency (inset in Fig.6 e) was maintained ~97 %, signifying that the CRGO-60 supercapacitor devices worked stably.

These superior capacitive behaviors can be attributed to the following aspects. First, significantly improved electronic conductivity due to the CO reduced and repaired. The high conductivity allowed the electrolyte ions to diffuse easily through the open pore channels of the CRGO. Such an improvement can also be ascribed to its highly porous structures and high surface areas by CO activation. Here, CO reduces the three main oxygen containing species that are present on GO by abstracting an oxygen atom. The reaction product is either CO_2 (for epoxides and ketone pairs), or CO_2 and H_2O (for hydroxyls). [47] Moreover, the resultant of CO_2 gas can activate the macroscopic GO architectures with high pores, which have been reported by Sol Yun et al. [48] The existence of porous structure facilitates ion and electron transports quickly during the charge/discharge processes. Therefore, their electrochemical properties are significantly improved.

The energy density (E) and power density (P) were calculated from galvanostatic

RSC Advances Accepted Manuscript

charge/discharge curves by the following equations:

$$E = \frac{C_s \cdot (\Delta V)^2}{7.2} \quad (5)$$

$$P = \frac{E \cdot 3600}{\Delta t} \quad (6)$$

where E is the energy density (Whkg^{-1}), P is the power density (kWkg^{-1}), C_s is the specific capacitance based on the mass of the electroactive material, V is the potential window of discharge (V), t is the discharge time (s). As is shown in Fig.6(f), the CRGO exhibits an energy density of 24.8 Whkg^{-1} at a power density of 500 Wkg^{-1}, which is in sharp contrast with 13.5 Whkg^{-1} in RGO. Even at a high power density of 20 kWkg^{-1}, the capacitor based CRGO still delivery an energy of 9.9 Whkg^{-1}. This value is in good agreement with its rectangular CV profile at high scan rate and good capacitance retention at high charging/discharging rate.[49, 50]

4. Conclusion

In conclusion, highly electrical conductivity and porous 3D graphene nanostructures were prepared by thermal annealing of GO in the presence of CO atmosphere. The obtained materials display a high surface area, great pore volume, and fewer defects which provide the ideal electrode materials for supercapacitors. As a result, a specific capacitance up to 291 Fg^{-1} at a current density of 1 Ag^{-1}, a high-rate performance and a good electrochemical cyclability were achieved in both three-electrode setup and two-electrode symmetrical configuration. This strategy has a great potential for the development and large-scale application of the advanced electrochemical energy storage devices.

Acknowledgements

RSC Advances Accepted Manuscript

The authors are grateful for support from the National Natural Science and Henan Province United Foundation of China (No.U1204601), National Natural Science Foundation of China (No.51302250 and 61274012), Natural Science Foundation of Zhengzhou City (No. 131PLJRC649 and 20130800).

References

1. J. R. Miller and P. Simon, *Science*, 2008, 321, 651.
2. M.J. Zhi, C.C. Xiang, J.T. Li, M. Li, N.Q. Wu. *Nanoscale*, 2013,**5**, 72-88
3. K.S. Novoselov, A.K. Geim, S.V.Morozov, D.Jiang, Y.Zhang, S. V. Dubonos, I. V. Grigorieva, and A. A. Firsov, *Science*, 2004, 306, 666-669.
4. D. W. Wang, F. Li, Z. G. Chen, G. Q. Lu, H. M. Cheng, *Chem. Mater.* 2008, 20 7195-7200.
5. S. Shiraishi, M. Kibe, T. Yokoyama, H. Kurihara, N. Patel, A. Oya, Y. Kaburagi, Y. Hishiyama, *Appl. Phys. A,* 2006,82 , 585-591.
6. J. Han, L. L. Zhang, S. Lee, J. Oh, K. Lee, J. R. Potts, J. Ji, X. Zhao, R. S. Ruoff, S. Park, *ACS Nano*, 2013,7,19-26.
7. D. Hulicova-Jurcakova, A. M. Puziy, Olga I. Poddubnaya, F. Suárez-García, J. M. D. Tascón, G. Q. Lu, *J. Am. Chem. Soc.* 2009, 131, 5026-5027.
8. F. W. Ma, H. Zhao, L. P. Sun, Q. Li, L. H. Huo, T. Xia, S. Gao, G. S. Pang, Z. Shi, S. H. Feng, *J. Mater. Chem.* 2012, 22, 13464-13468.
9. L. Zhao, L. Z. Fan, M. Q. Zhou, H. Guan, S. Y. Qiao, M. Antonietti, M. Titirici, *Adv. Mater.* 2010, 22, 5202-5206.
10. D. Hulicova-Jurcakova, M. Kodama, S. Shiraishi, H. Hatori, Z. H. Zhu, G. Q. Lu, *Adv. Funct. Mater.* 2009, 19,1800-1809.
11. B. Xu, S. S. Hou, G. P. Cao, F. Wu, Y. S. Yang, *J. Mater. Chem.* 2012, 22,19088-19093.
12. K. S. Kim, S. J. Park, *Electrochim. Acta,* 2012,78, 147-153.
13. L. F. Chen, X. D. Zhang, H. W. Liang, M. G. Kong, Q. F. Guan, P. Chen, Z. Y. Wu, S. H. Yu, *ACS Nano,* 2012,6, 7092-7102.

RSC Advances Accepted Manuscript

14. C. M. Chen, Q. Zhang, X. C. Zhao, B. S. Zhang, Q. Q. Kong, M. G. Yang, Q. H. Yang, M. Z. Wang, Y. G. Yang, R. Schlögl, D. S. Su, *J. Mater. Chem.* 2012, 22 ,14076-14084.
15. Y. C. Qiu, X. F. Zhang, S. H. Yang, *Phys. Chem. Chem. Phys.* 2011, 13, 12554-12558.
16. H. M. Jeong, J. W. Lee, W. H. Shin, Y. J. Choi, H. J. Shin, J. K. Kang, J. W. Choi, *Nano Lett.* 2011,11, 2472-2477.
17. L. Sun, L. Wang, C. G. Tian, T. X. Tan, Y. Xie, K. Y. Shi, M. Y. Li, H. G. Fu, *RSC Adv.* 2012, 2 ,4498-4506.
18. H. J. Wang, X. X. Sun, Z. H. Liu, and Z. B. Lei, *Nanoscale,* 2014, 6, 6577.
19. A. K. Geim and K. S. Novoselov, *Nat. Mater.*, 2007, 6, 183 -191
20. Y. Ohno, K. Maehashi, Y. Yamashiro and K. Matsumoto, *Nano. Lett.*, 2009, 9, 3318-3322.
21. H. Xu and K. S. Suslick, *J. Am. Chem. Soc.*, 2011, 133, 9148-9151.
22. R. Hao, W. Qian, L. Zhang and Y. Hou, *Chem. Commun.*, 2008, 45, 6576-6578.
23. A. Schlierf, H. Yang, E. Gebremedhn, E. Treossi, L. Ortolani, L. Chen, A. Minoia, V. Morandi, P. Samorì, C. Casiraghi, D Beljonne and V. Palermo, *Nanoscale,* 2013, 5, 4205-4216.
24. D. Antiohos, K. Pingmuang, M. S. Romano, S. Beirne, T. Romeo, P. Aitchison, A. Minett, G. Wallace, S. Phanichphant and J. Chen, *Electrochim. Acta*, 2013, 101, 99-108.
25. R. Ruoff, Nat. *Nanotechnol.*, 2008, 3, 10.
26. Y. Huang, J. Liang and Y. Chen, Small, 2012, 8, 1805.
27. M. F. El-Kady, V. Strong, S. Dubin and R. B. Kaner, *Science*, 2012, 335, 1326.
28. D. Li, M. B. Muller, S. Gilje, R. B. Kaner and G. G. Wallace, *Nat. Nanotechnol.*, 2008, 3, 101.
29. S. Yin, Z. Niu and X. Chen, *Small*, 2012, 8, 2458.
30. Y. Xu, K. Sheng, C. Li and G. Shi, *ACS Nano*, 2010, 4, 4324.
31. G. Ning, Z. Fan, G. Wang, J. Gao, W. Qian and F. Wei, *Chem. Commun.,* 2011, 47, 5976

RSC Advances Accepted Manuscript

32. H. Cao, X. Zhou, Z. Qin and Z. Liu, *Carbon*, 2013, 56, 218-223.
33. S. Guo and S. Dong, *Chem. Soc. Rev.*, 2011, 40, 2644-2672.
34. S. Guo, S. Dong and E. Wang, *ACS Nano*, 2010, 4, 547-555.
35. Y. Bai, R. B. Rakhi, W. Chen and H. N. Alshareef, *J. Power Sources*, 2013,233, 313-319
36. Y. N. Meng, Dr. K. Wang, Dr. Y. J. Zhang, Z. X. Wei. *Adv. Mater.* 2013, 25, 6985–6990
37. K. Gopalsamy , Z. Xu, B.N. Zheng, T.Q. Huang, L. Kou, X.L Zhao, C. Gao, *Nanoscale*, 2014,6, 8595-8600
38. H.J. Wang, X.X. Sun, Z. H. Liu, Z.B. Lei. *Nanoscale*, 2014, 6, 6577-6584.
39. H. F. Huang, L.Q. Xu, Y.M. Tang, S.L. Tang , Y.W. Du. *Nanoscale,* 2014, **6**, 2426-2433
40. J.L. Shi, W. Ch. Du, Y. X. Yin, Y. G. Guo, L.J. Wan. *J. Mater. Chem. A,* 2014,2, 10830-10834 .
41. B.G. Choi, M.Yang, W. H. Hong, J.W. Choi , Y. S. Huh, *ACS Nano*, 2012, 6, 4020 – 4028 .
42. X. Yang, J.Zhu , L. Qiu , D. Li , Adv. Mater. 2011, 23, 2833 –2838.
43. L.Dong, Z.X. Chen, D. Yang, H.B. Lu, *RSC Adv.*, 2013,**3**, 21183-21191
44. Y. B. Tan, J. M. Lee. *J. Mater. Chem. A*, 2013,**1**, 14814-14843 .
45. F. Zhang, T. F. Zhang, X. Yang, L. Zhang, K. Leng, Y. Huang, Y.S. Chen. *Energy Environ. Sci.,* 2013,**6**, 1623-1632
46. N. A. Kumar, J.-B. Baek, *Chem. Commun.*, 2014,**50**, 6298-6308
47. B. Narayanan, *J. Vac. Sci. Technol. A*, 2013, 31(4), 040601-8.
48. S. Yun, S –O. Kang, S. J. Park, H. S. Park. *Nanoscale*, 2014, 6, 10, 5296-5302.
49. L. Dong, Z. X. Chen, D. Yang and H. B. Lu, *RSC Adv.*, 2013, 3, 21183.
50. D. V. Shinde, D. Y. Lee, S. A. Patil, I. Lim, S. S. Bhande, W. Lee, M. M. Sung, R. S. Mane, N. K. Shrestha and S. H. Han, *RSC Adv.*, 2013, 3, 9431.

RSC Advances Accepted Manuscript